RSC Advances

ROYAL SOCIETY OF CHEMISTRY

www.rsc.org/advances

Formation mechanism and optical properties of $CdMoO_4$ and $CdMoO_4$: Ln^{3+} (Ln = Pr, Sm, Eu, Dy, Ho and Er) microspheres synthesized via a facile sonochemical route

Junjun Zhang[a], Nannan Zhang[a], Lianchun Zou[b,*], Shucai Gan[a,*]

[a] College of Chemistry, Jilin University, Changchun 130026, PR China

[b] Teaching Center of Basic Courses, Jilin University, Changchun 130062, PR China

* Corresponding author: E-mail: zoulianchun@126.com (L.C. Zou)

* Corresponding author: E-mail: gansc@jlu.edu.cn (S.C. Gan)

Abstract: In the present work, large-scale uniform $CdMoO_4$ and $CdMoO_4$: Ln^{3+} (Ln = Pr, Sm, Eu, Dy, Ho, Er) microspheres have been successfully synthesized via a facile sonochemical route. XRD, FE-SEM, EDS, the Brunauer-Emmett-Teller (BET) surface area, and photoluminescence (PL) spectra were used to characterize the samples. The results show that the $CdMoO_4$: Ln^{3+} can be directly indexed to tetragonal $CdMoO_4$ phase with high purity. The influence of the reaction time and reactants on the size and shapes of the $CdMoO_4$ microspheres had been studied, and the results revealed that the ultrasonic time and reactants play a crucial role in determining final morphologies of the samples. Additionally, the PL properties of $CdMoO_4$ and $CdMoO_4$: Ln^{3+} (Ln = Pr, Sm, Eu, Dy, Ho and Er) microspheres were investigated in detail. It can be seen that the $CdMoO_4$: Pr^{3+}, Sm^{3+}, Eu^{3+}, Dy^{3+}, Ho^{3+} and Er^{3+} samples are located in the red, yellow, red, white, yellow and green regions, respectively. Simultaneously, this novel and efficient pathway could open new opportunities for further investigating about the properties of molybdate materials.

Keywords: $CdMoO_4$; sonochemistry; microspheres; phosphor; luminescence

1. Introduction

Metal molybdates ($AMoO_4$, A = Ca, Sr, Ba, Pb and Cd) have novel properties and great potential applications in various fields such as PL, catalysis, scintillator materials, magnetic properties, and microwave applications [1-3]. Among these materials, cadmium molybdate is an important material owing to its excellent physical and chemical properties, electronic structure and relatively low band gap energy as compared to above scheelite structures. Cadmium molybdate is one of the metallic molybdate compounds with a scheelite structure and has a body-center orthorhombic unit cell with C_6^{4h} space group. Each site of Cd is surrounded by eight oxygen and Mo is surrounded by four equivalents oxygen [4]. This unique combination of physical and chemical properties of $CdMoO_4$ in term of molecular and electronic versatility, reactivity and stability suggests that a $CdMoO_4$ may be a promising substrate materials [5]. Therefore, it is of great importance to study the optical properties of this material for potential applications.

Fabrication of multi-dimensional (MD) hierarchical inorganic materials with highly specific size and morphology is a key aspect of modern materials science in many fields such as, advanced materials, catalysis, medicine, photoelectric material, ceramics, pigments, etc [6-8]. So far, some approaches have been demonstrated to be most effective for the preparation of multi-dimensional structures, such as sol-gel method, solvothermal route, microwave and microemulsion methods [9-12]. However, these methods tend to be rather complicated with obvious drawbacks of the final products and limit the practical applications. Large-scale use will require the development of simple low-cost approaches to the synthesis of inorganic functional materials. Therefore, it is still highly desirable to develop a facile, simple and mild method for the preparation of MD structure materials.

High intensity ultrasound has found many important applications in organic synthesis, materials and organometallic chemistry, and industrial manufacturing processes [13]. The chemical and physical effects of ultrasound therefore arise not from a direct interaction between chemical species and sound waves, but rather from the physical phenomenon of acoustic cavitation: the formation, growth, and implosive collapse of bubbles. Sonochemistry originates from the extreme transient conditions induced by ultrasound, which produces unique hot spots that can achieve temperatures above 5000 K, pressures exceeding 1000 atmospheres, and heating and cooling rates in excess of 10^{10} K s^{-1} [14-16]. These conditions are distinct from other conventional synthetic techniques such as photochemistry, wet chemistry, hydrothermal synthesis. To the best of our knowledge, the sonochemical approach for $CdMoO_4$ preparation has not yet been reported.

Herein, we employed a facile sonochemical route without using any catalysts or templates to prepare uniform and monodisperse $CdMoO_4$ and $CdMoO_4$:Ln^{3+} (Ln = Pr, Sm, Eu, Dy, Ho and Er) microspheres. In addition, the possible formation mechanism of the microspheres is proposed. The energy transfer process from host to rare earth ions were investigated systematically. Particularly, $CdMoO_4$: Ln^{3+} phosphors have controlled morphology and potential applications as an UV-convertible phosphors for LEDs. This work provides some insight into the design of other well-defined molybdate functional materials by sonochemistry synthesis.

2. Experimental section

2.1 Synthesis

$CdCl_2 \cdot 2.5H_2O$ (A. R.), $Cd(CH_3COO)_2 \cdot 2H_2O$ (A. R.), $(NH_4)_6Mo_7O_{24} \cdot 4H_2O$ (A. R.), $Na_2MoO_4 \cdot 2H_2O$ (A. R.), Pr_6O_{11} (99.99%), Ln_2O_3 (99.99%) (Ln = Sm, Eu, Dy, Ho Er) and absolute ethanol were purchased from Beijing Fine Chemicals Co. (China). Aqueous solutions of

$Ln(NO_3)_3$ were obtained by dissolving rare earth oxides in dilute HNO_3 solution under heating with agitation. All the reagents were used as-received without further purification.

In a typical procedure, 5 mmol (1.1417g) of $CdCl_2 \cdot 2.5H_2O$ was added into 25 mL of deionized water to form a solution (labeled as A). Meantime, the same amount of $Na_2MoO_4 \cdot 2H_2O$ (1.2097g) was added into 25 mL of deionized water to form a colorless solution (labeled as B). Then solution B was added dropwise to solution A under vigorous magnetic stirring, and a white precipitate was yielded immediately, and the suspension was labeled as C. After above process, the resulting precursor C was ultrasound irradiated for 30 min by an ordinary ultrasound cleaning bath. At the end of the sonication, a temperature of about 50□ was reached under ambient air without cooling. Subsequently, the products were separated from the solution by centrifugation, washed several times with deionized water and absolute ethanol to remove any ionic residual, and then dried in vacuum at 80□ for 12h. At last, the final $CdMoO_4$ samples were obtained and collected for characterizations. $CdMoO_4$:Ln^{3+} samples were prepared in a similar procedure except adding a stoichiometric amount (5 mol%) of $Ln(NO_3)_3$ together with $CdCl_2 \cdot 2.5H_2O$ were added as the initial materials, as described above. The specification of the ultrasound cleaning bath (Fig.S1) used are as follows: Manufacturer: KQ-300, Kunshan ultrasonic instrument co., LTD, China; Frequency: 40 kHz; Rated output power: 300 W [15].

2.2 Characterization

The samples were examined by XRD measurements performed on a Rigaku D/max-II B X-ray diffractometer with monochromatic Cu Kα radiation (k = 0.15406 nm). The XRD data were collected by using a scanning mode in the 2θ ranging from 10° to 80° with a scanning step size of 0.02° and a scanning rate of 4.0° min^{-1}. SEM images and EDS of the products were obtained on

field emission scanning electron microscope (Hitachi S-4800, Japan), employing an accelerating voltage of 5 kV or 15 kV. The FT-IR spectroscopy (Iraffinity-1, Shimadzu, Japan) was used to confirm the surface chemical structure of the products in the wave number range of 400-4000 cm^{-1} by KBr disk method. The Brunauer-Emmett-Teller (BET) specific surface area (SSA) of the powders was analyzed by nitrogen adsorption on a Micromeritics ASAP 2020 nitrogen adsorption apparatus (U.S.A.). Before nitrogen adsorption measurement, the sample was degassed in vacuum at 180 ^{o}C for 2 h. The PL excitation and emission spectra were recorded with a Hitachi F-7000 spectrophotometer equipped with a 150W Xe lamp as the excitation source. The quantum efficiency (QE) was measured using the integrating sphere on the time resolved and steady state fluorescence spectrometers (FLS920, Edinburgh Instruments), and a Xe900 lamp was used as an excitation source. In addition to the BET surface area, all of the measurements were performed at room temperature.

3. Results and discussion

3.1. The basis of characterizations of the as-prepared $CdMoO_4$ samples

X-ray diffraction analysis was used to examine the crystal structure of the products. The XRD pattern of the as-prepared $CdMoO_4$ product was shown in Fig.1a. All of the observed diffraction peaks can be perfectly indexed to those of the tetragonal phase of $CdMoO_4$ with cell constants of a = 5.155Å and c = 11.194Å (JCPDS No. 07-0209) [17]. No additional peaks of other phases have been found, indicating the formation of a pure single phase can be easily obtained by this method. And the sharp strong diffraction peaks indicate the good crystallinity of the as-synthesized products. The EDS spectrum shows strong peaks of Cd, Mo and O (Fig. 1b). No other impurity peaks can be detected, which confirms the pure phase of $CdMoO_4$ and can effectively support the

XRD result of the samples. Quantitative analysis shows that the atom ratio of Cd:Mo:O is about 1:1:4, giving a stoichiometric composition of $CdMoO_4$. The analysis of EDS shows that the $CdMoO_4$ has been prepared successfully by sonochemistry method.

The nitrogen adsorption-desorption isotherm and pore-size distribution curve were investigated to evaluate the surface area and pore size distribution of the $CdMoO_4$ microspheres. As seen in Fig. 1c, the N_2 adsorption-desorption isotherm can be identified as type IV in the IUPAC (International Union of Pure and Applied Chemistry) classification with a distinct hysteresis loop. The hysteresis loop in the low relative (P/P_0) range of 0.5-1 may be ascribed to the presence of mesopores as well as macropores on the surface of the microspheres. The pore volumes and BET specific surface area are about 0.013 $cm^3 \cdot g^{-1}$ and 1.34 m^2/g of the $CdMoO_4$ microspheres, respectively . Combined with the Barrett-Joyner-Halenda (BJH) pore size distribution (Fig.1d), the $CdMoO_4$ microspheres exhibit hierarchical porosity: mesopores (2-50 nm) together with macropores (>50 nm) [30].

FT-IR spectroscopy was performed on the as-prepared $CdMoO_4$ sample, as illustrated in Fig. S2. The bands at 435, 771, 1651 and 2360 cm^{-1} are observed. The absorption band at 435 cm^{-1} has been attributed to the bending vibration of Mo-O. A strong absorption band at 771cm^{-1} is related to O-Mo-O stretches of the MoO_4 tetrahedron [18]. This implies that the crystalline $CdMoO_4$ phase has formed in the as-prepared particles. The absorption band centered at 2360 cm^{-1} is assigned to the CO_2 on the surface of the sample. The absorption band located at 1651 cm^{-1} can be ascribed to the O-H bending vibration of water adsorbed on the surface of the samples [19]. Because the samples were prepared in aqueous solution, the surface of particles can be covered inevitably with the absorbed water molecules. The FT-IR result provides additional evidence for the formation of

the $CdMoO_4$ product after the sonochemical process, which is in good accordance with the XRD and EDS results.

It should be emphasized that doping a small amount of Ln^{3+} (Ln = Pr, Sm, Eu, Dy, Ho, Er) in the $CdMoO_4$ host does not change the phase, crystallization, and morphology of the $CdMoO_4$ products in our present study, which agrees well with the previous literatures [34, 44]. Therefore, here we only choose pure $CdMoO_4$ host as an example to illustrate the morphology of the samples. The morphology of the obtained $CdMoO_4$ sample was examined by FE-SEM. Fig. 2a shows FE-SEM image of the sample obtained under ultrasonic reaction for 30 min. The sample is composed of microspheres with a diameter of 2-3 μm. A high-magnification SEM image (Fig. 2b) reveals that microspheres is composed of tens of irregular nanoparticles (NPs). The device fabricated using spherical shaped particles should enhance the screen brightness and improve the resolution due to lower scattering of the emitted light and higher packing densities over irregular shaped particles. So our product may have great potential applications in the LEDs field [1, 34].

It was found that samples sizes, morphologies could be greatly influenced via the types of the reactants. We found that the Mo and Cd sources are critical to the formation of the microspheres structures. The XRD patterns of the as-prepared $CdMoO_4$ products obtained by means of different types of reactants were shown in Fig. S3. All of the observed diffraction peaks can be perfectly indexed to those of the tetragonal phase of $CdMoO_4$. Replacing $Na_2MoO_4{\cdot}2H_2O$ with $(NH_4)_6Mo_7O_{24}{\cdot}4H_2O$ as the Mo source while keeping the other reaction conditions the same results in the formation of rugby-like microstructures, as shown in Fig. 3 (a-d). The rugby-like structures have thickness of 1μm and diameters of 2 μm (Fig. 3c). Fig. 3d reveals that rugby-like microstructures is composed of myriad nanoparticles with size of circa 60-100nm. Replacing

$CdCl_2 \cdot 2.5H_2O$ with $Cd(CH_3COO)_2 \cdot 2H_2O$ as the Cd source while keeping the other reaction conditions the same results in the formation of small size microspheres, as shown in Fig. 3e. The size of the microspheres dropped to 1 μm (Fig. 3f). Comparing the two types of Mo sources, using $Na_2MoO_4 \cdot 2H_2O$ as the precursor might have the advantage of relatively fast release of MoO_4^{2-} ions so that the reaction kinetics favors the generation of $CdMoO_4$ microspheres. Comparing the two types of Cd sources, The microspheres obtained from $CdCl_2 \cdot 2.5H_2O$ (Fig. 2) have larger particle size than those obtained from $Cd(CH_3COO)_2 \cdot 2H_2O$. The CH_3COO^- ligand in $Cd(CH_3COO)_2 \cdot 2H_2O$, can act as a surfactant and provide steric hindrance. It is obvious that using $Cd(CH_3COO)_2 \cdot 2H_2O$ as Cd source results in microspheres structures formation with small size [20]. Through the transformation of reactants (Mo and Cd sources) can be found that the control of microspheres morphology are greatly influenced by Mo source. And the control of microspheres size are greatly influenced by Cd source.

In order to monitor the effect of the concentration of reactants on the size and morphology, we change the concentration of reactants from $[Cd^{2+}] = [MoO_4^{2-}] = 0.02$ M to $[Cd^{2+}] = [MoO_4^{2-}] = 0.14$ M. As shown in Fig. 4, it can be seen that the as-obtained products are mainly composed of large scale microspheres, implying that a high yield can be realized in the adopted reaction conditions. We found that with the change of concentration of reactants, the product can maintain the spherical morphology. By careful observation, the concentration of reactants have a great influence on the uniformity and monodispersity of $CdMoO_4$ microspheres. Too high or too low of the concentration of reactants are not conducive to fine morphology. Thus, choosing an optimal condition ($[Cd^{2+}] = [MoO_4^{2-}] = 0.10$ M) is of substantial importance to synthesize $CdMoO_4$ with an ideally spherical shape, narrow size distribution, and showing low-agglomeration.

3.2 Formation mechanism research based on time-dependent experiments

To investigate the details of the sonochemical conversion from precursor to final products, we have carried out a series of experiments by employing different sonication times without changing other preparation conditions. Fig. 5 (a-f) represent the SEM images of the precursor intermediates obtained at different reaction periods of 0 (a), 5 (b), 10 (c), 15 (d), 20 (e) and 30 min (f), respectively. When the reaction was performed in the absence ultrasonic irradiation, the product is only composed of amorphous nano-/micron-blocks without a discernable morphology (Fig. 5a). After ultrasonic reaction for 5 min, the nano-/micron-blocks become NPs, and some microspheres architectures could occasionally be observed, but there are still some NPs left as shown in Fig. 5b. As the reaction went on, more and more well-defined microspheres were generated though some NPs still existed in the product (Fig. 5c-e). As illustrated in Fig. 5f, a longer reaction time of 30 min gave rise to an increase in the number of microspheres, and microspheres became the predominant product. Therefore, the experiments have proved that ultrasonic irradiation played an important role in the formation of $CdMoO_4$ microspheres. The XRD patterns of the products were collected at different reaction stages are provided in the Fig. S4. It can be seen that all the diffraction peaks can be indexed into the pure tetragonal phase and no trace of additional peaks from other phases can be detected, implying that the samples are of high purity.

On the basis of the above experimental process, the possible formation mechanism of such $CdMoO_4$ microspheres structures could be carefully elucidated as follows. We believe that the sonochemical formation of 3D $CdMoO_4$ microspheres structure by means of "dissolution & recrystallization - growth - self-assembled". A possible reaction scheme of the formation process for $CdMoO_4$ can be summarized as follows [21]:

$$CdCl_2 \cdot 2.5H_2O \rightarrow Cd^{2+} + 2Cl^- + 2.5H_2O \quad (1)$$

$$Na_2MoO_4 \cdot 2H_2O \rightarrow 2Na^+ + MoO_4^{2-} + 2H_2O \quad (2)$$

$$Cd^{2+} + MoO_4^{2-} \rightarrow CdMoO_4 \downarrow \quad (3)$$

At first, the reactants $CdCl_2 \cdot 2.5H_2O$ and $Na_2MoO_4 \cdot 2H_2O$ were dissolved in the aqueous solution (Eq. 1 and Eq. 2). When a Na_2MoO_4 solution is added to $CdCl_2 \cdot 2.5H_2O$ solution, free Cd^{2+} ions can react with the vicinal MoO_4^{2-} to form numerous tiny $CdMoO_4$ crystalline nuclei, which led to the formation of $CdMoO_4$ nano-/micron-blocks (Eq. 3) [13]. The small K_{sp} (solubility product constant) of $CdMoO_4$ drives the whole reaction, which can be seen as internal driving force for reaction [22]. When the solution is irradiated by high intensity of ultrasound, acoustic cavitation in reaction system occurs. Bubbles collapse in liquid and produce enormous amount of heat energy. Meanwhile, ultrasound irradiation will generate strong tiny jets in water and facilitate the nanoparticles to distribute uniformly [23]. Therefore the $CdMoO_4$ nano-/micron-blocks would crack into small nanoparticles and further disperses in the presence of the strong shock wave of the ultrasound through a dissolution & recrystallization process, which led to the growth of $CdMoO_4$ nanoparticles [24]. Sonication was helpful to obtain relatively small and uniform particles. The same observation have been reported in the previous literature [25, 26].The small nanoparticles are aggregated into nanoparticles via a process known as growth involving coarsening [27]. And these nanoparticles further assembled into microspheres structure to reduce the surface area and energy [28]. A plausible formation mechanism of self-assembled $CdMoO_4$ microspheres is illustrated in Fig. 6.

3.3 Optical properties of $CdMoO_4$ host and $CdMoO_4:Ln^{3+}$ phosphors

Molybdate compounds have been shown to be an efficient host lattice for Ln^{3+}, bringing about all kinds of PL properties. As we known, MoO_4^{2-} group has excellent absorption in the near UV

region. Hence, the energy transfer process from MoO_4^{2-} to Ln^{3+} can easily occur, which can greatly enhance the PL efficiency of Ln^{3+} doped materials [29]. To our knowledge, the PL properties of $CdMoO_4$:Ln^{3+}(Ln = Pr, Sm, Eu, Dy, Ho, Er) which obtained through sonochemical approach have been rarely investigated yet.

Fig. 7a shows the UV-vis absorbance spectrum of $CdMoO_4$ sample. The sample has a broad band range from 200 to 385 nm, which is due to the O-Mo charge transfer transitions (CTT) of MoO_4^{2-} groups. The steep shape of the spectrum indicated that the absorption was not due to the transition from the impurity level but the band-gap transition [16, 30]. The combination between absorbance and PL measurements allows to discover the energy levels in the materials and the optical band gap value. The optical band gap energy (E_{gap}) was calculated by the method proposed by Wood and Tauc. According to reference [31], the optical band gap is associated with absorbance and photon energy by the following equation (Eq):

$$h\nu\alpha \square (h\nu - E_{gap})^n$$

where a is the absorbance, h is the Planck constant, ν is the frequency, E_{gap} is the optical band gap, and n is a constant associated with the different types of electronic transitions (For n = 1/2, 2, 3/2 and 3, the transitions are the direct allowed, indirect allowed, direct forbidden, and indirect forbidden, respectively.). According to Lacomba-Perales et al. the molybdates with scheelite-type tetragonal structure present a direct allowed electronic transition [32]. So, in our study, n = 1/2 was chosen as the criterion in Eq. The plot of $(AE_{photon})^2$ versus E_{photon} is shown in Fig. 7b. The E_{gap} value of $CdMoO_4$ was evaluated extrapolating the linear portion of the curve or tail. UV-vis measurements on the sample showed a typical value of 3.38 eV.

PL properties of these $CdMoO_4$ microspheres are being studied. Fig. 8 shows the PL spectra of

the $CdMoO_4$ samples obtained under different reactants (a) $CdCl_2 \cdot 2.5H_2O + Na_2MoO_4 \cdot 2H_2O$ (b) $Cd(CH_3COO)_2 \cdot 2H_2O + Na_2MoO_4 \cdot 2H_2O$ (c) $CdCl_2 \cdot 2.5H_2O + (NH_4)_6Mo_7O_{24} \cdot 4H_2O$, respectively. With excitation at 330 nm, the spectra show that all the three samples exhibited broad emission band peaks at 470 nm, which is mainly attributed to the charge transfer transition (CTT) between the O 2p orbitals and the Mo 4d orbitals within the MoO_4^{2-} complex [1]. It is commonly accepted that the PL properties of inorganic materials are strongly dependent on their sizes, morphologies, and crystallinity. From Fig. 8, it can be clearly seen that the emission spectra of the products synthesized at different reactants are similar in shape, but different in the intensity to some extent, indicating that the luminescent properties are closely correlated with the morphologies and sizes of the materials. Under identical measurement conditions, the microspheres (black line) have the highest relative emission intensity, while the rugby-shaped structures exhibit the lowest intensity. It is thus inferred that the morphology of the 3D microspheres (large size) is more beneficial than the morphology of rugby-shaped and microspheres (small size) to the emission. The possible reasons for the different of emission intensities can be deduced as follows. On the one hand, the microspheres (large size) has an average diameter of 2-3 μm, which is much bigger than the rest of microstructures. The enhanced luminescence performance due to microspheres (large size) has less surface defect than the other samples. On the other hand, the electronic structures could be modified by means of the changes of the sizes and shapes of samples, which influences the excitation of the carriers from the valence band to the conduction band and the numbers of photons released from the surfaces of samples [6, 15]. Compared to the previous reported PL spectrum of $CdMoO_4$ nano-octahedra with the edge length of about 25 nm, our sample has a red shift of approximately 30 nm. It is obvious that the $CdMoO_4$ microspheres possess higher specific

surface areas than that of $CdMoO_4$ nano-octahedra due to their complex morphology, which might lead to the red shift of the luminescence peak [17]. All of the aforementioned observations support the concept of morphology-dependent properties of $CdMoO_4$ samples and emphasize the importance of morphology and size control.

As an example of latent application, various lanthanide ions (Ln^{3+}: Ln = Pr, Sm, Eu, Dy, Ho and Er) have been doped into the microspheres and the corresponding PL properties were investigated in detail. As demonstrated by XRD patterns of the as-synthesized samples doped with different types of Ln^{3+} shown in Fig. S5. One can see that the diffraction peaks of $CdMoO_4$:Ln^{3+} samples agree well with tetragonal scheelite-type $CdMoO_4$, indicating that the Ln^{3+} (Ln = Pr, Sm, Eu, Dy, Ho, Er) ions have been effectively doped into the $CdMoO_4$ host lattice.

Fig. 9 presents the excitation and emission spectra of the $CdMoO_4$: Ln^{3+} (Ln = Pr, Sm, Eu, Dy, Ho and Er) samples. The excitation and emission spectra of the $CdMoO_4$:Pr^{3+} phosphor at room temperature are given in Fig.9 (a, b). In the excitation spectra monitored at 606 nm, a broad band with a maximum at 322 nm can be observed, which can be assigned to the CTB from the oxygen ligands to the central molybdates atom within the MoO_4^{2-} groups. As shown in Fig. 9a, it can be seen that some sharp lines are in the 400-500 nm long wavelength range, including 453 nm ($^3H_4 \rightarrow {}^3P_2$), 477 nm ($^3H_4 \rightarrow {}^3P_1$), and 490 nm ($^3H_4 \rightarrow {}^3P_0$), respectively [33]. Upon excitation into the MoO_4^{2-} group at 322 nm, the characteristic emission spectra of the Pr^{3+} ions at 534 nm ($^3P_0 \rightarrow {}^3H_4$), 561 nm ($^3P_0 \rightarrow {}^3H_5$), 597 and 606 nm ($^1D_2 \rightarrow {}^3H_4$), 623 nm ($^3P_0 \rightarrow {}^3H_6$) and 654 nm ($^3P_0 \rightarrow {}^3F_2$) can be detected (Fig. 9b).

Sm^{3+} ions with $4f^5$ configuration has complicated energy levels and various possible transitions of f-f levels. The transitions between these f-f levels are highly selective and of sharp line spectra

[34]. The excitation and emission spectra of $CdMoO_4:Sm^{3+}$ are depicted in Fig.9 (c, d). The intense and broad absorption band centered at 339 nm is assigned to the combination of the CTB of $O^{2-}\rightarrow Mo^{6+}$ and Sm^{3+} in MoO_4^{2-} group. All the sharp peaks of the excitation spectra are due to the excitation from ground-level $^6H_{5/2}$ to higher energy levels of Sm^{3+} ion. As shown in Fig. 9c, it can be seen that some sharp lines are in the 390-500 nm wavelength range, including 408 nm ($^6H_{5/2}\rightarrow{}^4K_{11/2}$), 423 nm ($^6H_{5/2}\rightarrow{}^6P_{5/2} + {}^4M_{19/2}$), 478 nm ($^6H_{5/2}\rightarrow{}^4I_{11/2} + {}^4M_{15/2}$), respectively. The strongest excitation sharp line is corresponding to $^6H_{5/2}$–$^4K_{11/2}$ transition of Sm^{3+} located at 408 nm. The emission spectrum of $CdMoO_4:Sm^{3+}$ consists of three sharp peaks in the visible region near 563, 596 and 606, 645 nm, which are assigned to the intra-4f-shell transitions from the excited level $^4G_{5/2}$ to ground levels $^6H_{5/2}$, $^6H_{7/2}$, $^6H_{9/2}$, respectively (Fig. 9d). The strongest emission peak located at 563 nm is originated from $^4G_{5/2}\rightarrow{}^6H_{5/2}$ typical transition of Sm^{3+} [35].

Fig. 9 (e f) illustrate the excitation (λ_{em} = 615 nm) and emission (λ_{ex} = 330 nm) spectra of the $CdMoO_4:Eu^{3+}$ phosphor. From Fig. 9e, the intense and broad absorption band centered at 330 nm is assigned to the combination of the CTB transitions of $O^{2-}\rightarrow Mo^{6+}$ and $O^{2-}\rightarrow Eu^{3+}$ groups [4, 36]. As shown in Fig. 9e, it can be seen that some sharp lines are in the 370-500 nm long wavelength range, including 382 ($^7F_0\rightarrow{}^5L_7$), 395 ($^7F_0\rightarrow{}^5L_6$), 417 ($^7F_0\rightarrow{}^5D_3$), 467 nm ($^7F_0\rightarrow{}^5D_2$), respectively. The broad excitation band is ascribed to the intra-configurational 4f-4f transitions of Eu^{3+} in the host lattices. Two of the strongest absorptions are at 395 nm ($^7F_0\rightarrow{}^5L_6$) and 467 nm ($^7F_0\rightarrow{}^5D_2$), respectively. As shown in Fig.9f, the main emission at 615 nm, originating from the electric dipole transitions and hypersensitive to the environment of Eu^{3+}, other f-f transitions of Eu^{3+} ion, such as 591 and 650nm, relatively weak, which are associated with the $^5D_0\rightarrow{}^7F_1$ and $^5D_0\rightarrow{}^7F_3$, respectively [36, 37]. When excited by 330, 395 and 467 nm, the emissions of the phosphor are

shown in Fig. S6, respectively. The emission intensities decrease with increasing the excitation wavelength. It should be noticed that the red emission intensity excited at 330 nm is far greater than that of excited at near-UV radiation (395 nm) and blue region 467 nm, suggesting that the energy transfer from MoO_4^{2-} to Eu^{3+} is very efficient. When the excitation wavelength is 330nm, our sample is twice the intensity of the commercial phosphor Y_2O_3:Eu^{3+} (Grirem Advanced Materials Co., Ltd.). Compared withY_2O_3:Eu^{3+} phosphor, $CdMoO_4$:Eu^{3+} is much more stable, efficient and suitable, therefore, $CdMoO_4$:Eu^{3+} may have potential application as a red phosphor in the LEDs field (Fig. S7). The quantum efficiency of the phosphor is measured by the integrated sphere method and can be calculated according to the equation $Q = (E_c - (1 - A))\cdot E_b / L_a \cdot A$, where E_c is the integrated luminescence of the powder caused by direct excitation, E_b is the integrated luminescence of the powder caused by indirect illumination from the sphere and the term L_a is the integrated excitation profile from an empty integrated sphere (blank control). A is the powder absorbance. [38] The quantum efficiency for the $CdMoO_4$:$0.05Eu^{3+}$ phosphor with 330 nm excitation were calculated by integrating emission counts from the 550 to 650 nm wavelength range. The values is found to be about 43.94%. The values is higher than that of the commercial red-emittingY_2O_3:Eu^{3+} (12.2%) and Y_2O_2S:Eu^{3+} (35.0%), respectively. [39, 40] Thus, the $CdMoO_4$:$0.05Eu^{3+}$ phosphor demonstrates a high quantum efficiency and potential application

Fig. 9 (g, h) shows the excitation and emission spectra of $CdMoO_4$: Dy^{3+} phosphor. The broadband centered at 330 nm is attributed to a CTB, which occurs by electron delocalization from $O^{2-} \rightarrow Mo^{6+}$ and $O^{2-} \rightarrow Dy^{3+}$ in MoO_4^{2-}. There are some sharp lines between 340 and 500 nm, which correspond to f-f transitions within Dy^{3+}. The excitation peaks locate at 353, 368, 391, 429, 455 and 477 nm, which are attributed to the transitions from the $^6H_{15/2}$ ground state to $^6P_{7/2}$, $^6P_{5/2}$,

$^4F_{7/2}$ + $^4I_{13/2}$, $^4G_{11/2}$, $^4I_{15/2}$, and $^4F_{2/9}$ respectively [41]. The emission spectrum is composed of two groups of narrow bands and the emission peaks are located at 478, 487 and 575nm (Fig. 9h). The emission corresponds to the $^4F_{9/2}$→$^6H_{15/2}$ (478 and 487 nm) and $^4F_{9/2}$→$^6H_{13/2}$ (575 nm) transitions of Dy^{3+}. In $CdMoO_4$ host, if Dy^{3+} occupies an inversion symmetry site in the crystal lattice, the magnetic dipole transition is the dominant transition. while the electric dipole transition will be the dominant transition if Dy^{3+} occupies an unsymmetrical site in the crystal lattice [42]. The $^4F_{9/2}$→ $^6H_{13/2}$ transition of Dy^{3+} belongs to electric dipole transitions and $^4F_{9/2}$→$^6H_{15/2}$ transition belongs to magnetic dipole transitions. It can be seen from Fig. 9h that the strong yellow emission line at 575 nm ($^4F_{9/2}$→$^6H_{13/2}$) is the dominant band, which indicates that Dy^{3+} ions do not occupy the inversion symmetry site.

Fig. 10a exhibits the emission spectrum of $CdMoO_4$: Ho^{3+} sample. The emission spectrum is composed of two groups of bands and the emission peaks are located at 543, 644 and 660nm. The emission corresponds to the $^5F_4$→$^5I_8$ (543nm) and $^5F_5$→$^5I_8$ (644 and 660nm) transitions of Ho^{3+}, respectively [43]. Fig. S8a shows the excitation of $CdMoO_4$:Ho^{3+} phosphor. The broadband centered at 320 nm is attributed to a CTB, which occurs by electron delocalization from O^{2-} to Mo^{6+} and Ho^{3+} in MoO_4^{2-}. There are some sharp lines between 350 and 500 nm, which correspond to f-f transitions within Ho^{3+}. The excitation peaks locate at 361, 402, 418, 451and 481 nm, which are attributed to the transitions from the $^5I_8$ ground state to $^5G_2$, $^5G_4$, $^5G_5$, $^5F_1$ and $^5F_2$ respectively [44]. Fig. 10b exhibits the emission spectrum of $CdMoO_4$:Er^{3+} sample. The emission spectrum is composed of three groups of bands and the emission peaks are located at 525, 531, 545, 554 656 and 668 nm. The emission corresponds to the $^2H_{11/2}$→$^4I_{15/2}$ (525 and 531), $^4S_{3/2}$→$^4I_{15/2}$ (545 and 554) and $^4F_{9/2}$→$^4I_{15/2}$ (656 and 668) transitions of Er^{3+}, respectively [45]. Fig. S8b shows the

excitation of $CdMoO_4:Er^{3+}$ phosphor. The broadband centered at 318 nm is attributed to a CTB, which occurs by electron delocalization from O^{2-} to Mo^{6+} and Er^{3+} in MoO_4^{2-}. There are some sharp lines between 350 and 500 nm, which correspond to f-f transitions within Er^{3+}. The excitation peaks locate at 365, 378, 407and 488 nm, which are attributed to the transitions from the $^4I_{15/2}$ ground state to $^4G_{7/2}$, $^4G_{11/2}$, $^2H_{9/2}$, and $^4F_{7/2}$, respectively [46].

According to the excitation and emission spectra of $CdMoO_4$: Ln^{3+} (Ln = Pr, Sm, Eu, Dy, Ho, Er), the broad band originating from the molybdate hosts is predominant of all excitation spectra monitored at the prominent characteristic emissions of Ln^{3+} (Ln = Pr, Sm, Eu, Dy, Ho, Er), indicating that the doped Ln^{3+} ions can be excited through host absorption and the corresponding energy transfer process is highly efficient. This suggests the tetragonal $CdMoO_4$ is ideal host material for the luminescence of Ln^{3+} cations. To help explain the mechanism of multi-colour emission and the paths of energy transfer during PL, a schematic diagram is shown in Fig. 11 [47]. In the first place, the electrons of the host are first excited from the $^1A_1$ ground state to the $^1T_2$ excited state by absorbing ultraviolet radiation. Subsequently, when Ln^{3+} (Ln = Pr, Sm, Eu, Dy, Ho and Er) were incorporated into the host of $CdMoO_4$, the energy transfer from MoO_4^{2-} to Ln^{3+}. In the end, the energy can non-radiatively relaxes from high energy levels to the lower excited energy levels by multi-phonon relaxation. And the multi-colour emissions occur through representative transitions of Ln^{3+} [48, 49]. Based on the detailed PL analysis above, a conclusion can be drawn that $CdMoO_4$ is efficient host to sensitize Ln^{3+}. Meanwhile, sonochemical route is more convenient and could save time and energy for the synthesis of luminescent materials.

Chromaticity coordinates are one of the vital factors for evaluating performance of the prepared phosphors. We investigated the PL color of the as-obtained samples by using the 1931 CIE

(Commission Internationale de L'Eclairage) system. Fig. 12 presents the corresponding CIE coordinates positions, which show the different emission colors for the as-synthesized $CdMoO_4$: (A) Pr^{3+}, (B) Sm^{3+}, (C) Eu^{3+}, (D) Dy^{3+}, (E) Ho^{3+} and (F) Er^{3+} respectively. It can be seen that the $CdMoO_4$: (A) Pr^{3+}, (B) Sm^{3+}, (C) Eu^{3+}, (D) Dy^{3+}, (E) Ho^{3+} and (F) Er^{3+} samples are located in the red, yellow, red, white, yellow and green regions, respectively. A detailed conclusion for the excitation and emission peaks, CIE coordinates, colors and correlated color temperature (CCT) are listed in Table 1.

4. Conclusions

In summary, the present work provides an efficient sonochemistry process for the fabrication of novel 3D architectures of $CdMoO_4$ and $CdMoO_4$:Ln^{3+} microspheres. The investigation of synthesis parameters reveals that the ultrasonic time in the reaction system should be responsible for the formation of the $CdMoO_4$ microspheres. The reasonable formation mechanism of the microspheres was proposed on the basis of time-dependent experiments. PL spectra of $CdMoO_4$ show that the optical properties could be modulated through different morphologies and sizes. The as-prepared $CdMoO_4$:Ln^{3+} phosphors show abundant and excellent luminescent properties after incorporating Ln^{3+} cations under ultraviolet light excitation, which have potential applications in advanced flat panel displays and light emitting diodes. Notably, the results show that it is possible to design and synthesize microspheres by sonochemistry method. And the work can also be extended to other well-defined molybdate functional materials with controllable morphologies in the absence of any surfactants and templates.

Electronic Supporting Information: Fig. S1. Schematic illustration for reaction system and equipment. **Fig. S2.** FT-IR spectrum of CdMoO4 samples. **Fig. S3.** XRD patterns of $CdMoO_4$

obtained by using different reactants. (A = $CdCl_2 \cdot 2.5H_2O$; B = $Na_2MoO_4 \cdot 2H_2O$; C = $(NH_4)_6Mo_7O_{24} \cdot 4H_2O$; D = $(CH_3COO)_2Cd \cdot 2H_2O$).**Fig. S4.** XRD patterns of samples at different reaction time (a) 0, (b) 5, (c) 10, (d) 15 , (e) 20 min and (f) 30min, respectively. **Fig. S5.** XRD patterns of $CdMoO_4$: (a)Pr^{3+},(b)Sm^{3+}, (c)Eu^{3+}, (d)Dy^{3+}, (e)Ho^{3+} and (f)Er^{3+} phosphors. **Fig.S6.** Emission spectra of $CdMoO_4$:Eu^{3+} sample under 330, 395 and 467 nm wavelength excitation. **Fig.S7.** Emission spectra of $CdMoO_4$:Eu^{3+} compared with commercial red phosphor Y_2O_3:Eu^{3+} **Fig. S8.** Excitation spectra of $CdMoO_4$:Ho^{3+} (a) $CdMoO_4$:Er^{3+} (b) samples.

Acknowledgments

This present work was financially supported by Mineral and Ore resources Comprehensive Utilization of Advanced Technology Popularization and Practical Research (No. 12120113088300); And the Key Technology and Equipment of Efficient Utilization of Oil Shale Resources (No: OSR-5); The authors thank Bingnan Wang and Shasha Yi for their cooperation and kind help.

References

[1] C. Zhang, L. Zhang, C. Song, G. Jia, S. Huo, S. Shen, J. Alloys Compd., 2014, 589, 185-191

[2] X. Li, L. Guan, M. Sun, H. Liu, Z. Yang, Q. Guo, G. Fu, J. Lumin., 2011, 113, 1022-1025

[3] J. C. Sczancoski, M. D. R. Bomio, L. S. Cavalcante, M. R. Joya, P. S. Pizani, J. A. Varela, E. Longo, M. Siu Li, and J. A. Andrés, J. Phys. Chem. C, 2009, 113, 5812-5822

[4] W. Wang, L. Zhen, C. Xu, W. Shao, Z. Chen, J. Alloys Compd. 2012, 529, 17-20

[5] J. Lin, Z. Zeng, Q. Wang, Inorg. Chim. Acta, 2013, 408, 59-63

[6] W. Wang, L. Zhen, C. Xu, and W. Shao, Cryst. Growth Des., 2009, 9, 1558-1568

[7] T. D. Nguyen, D. Mrabet, C. T. Dinh and T. O. Do, CrystEngComm, 2011, 13, 1450-1460

[8] L. Zhang, X. Cao, Y. Ma, X.Chen and Z. Xue, New J. Chem. 2010, 34, 2027-2033

[9] C. Zhang, Y. Zhang, J. Wang, D. Wang, D. He, Y. Xia, J. Power Sources, 2013, 236, 118-125

[10] J. Yin, F. Gao, J. Wang and Q. Lu, Chem. Commun. 2011, 47, 4141-4143

[11] L. Zhang, X. Cao, Y. Ma, X. Chen and Z. Xue, CrystEngComm, 2010, 12, 207-210

[12] D. Chen, G. Shen, K. Tang, Z. Liang, and H. Zheng, J. Phys. Chem. B, 2004, 108, 11280-11284

[13] H. Xu, B. W. Zeiger and K. S. Suslick, Chem. Soc. Rev., 2013, 42, 2555-2567

[14] L. Mao, J. Liu, S. Zhu, D. Zhang, Z. Chen, C. Chen, Ultrason. Sonochem., 2014, 21, 527-534

[15] J. Zhang, L. Zou, S. Gan, G. Ji, J. Phys. Chem. Solids., 2014, 75, 878-887

[16] L. Liu, Y. Zhang, W. Tan, Ultrason. Sonochem., 2014, 21, 970-974

[17] Y. Li, S. Tan, J. Jiang, Z. Huang and X. Tan, CrystEngComm, 2011, 13, 2649-2655

[18] F Lei, B. Yan, J. Solid State Chem., 2008, 181, 855-862

[19] K. G. Sharma, N. R. Singh, J. Rare Earths, 2012, 30, 310-314

[20] Shahri, A. Sobhani, M. Salavati-Niasari, Mater. Res. Bul, 2013, 48, 3901-3909

[21] Y. Ni, G. Li, J. Hong, Ultrason. Sonochem. 2010, 17, 509-514

[22] J.P. Ge, Y.D. Li and G.Q.Yang, Chem. Commun. 2002, 17, 1826-1827

[23] B. Zhou, B. Liu, L. Jiang, J. Zhu, Ultrason. Sonochem.2007, 14, 229-234

[24] L. Xu, C. Lu, Z. Zhang, X. Yang and W. Hou, Nanoscale, 2010, 2, 995-1005

[25] P. Jeevanandam, Y. Diamant, M. Motiei and A. Gedanken, Phys. Chem. Chem. Phys., 2001, 3, 4107-411

[26] K. S. Suslick, Y. Didenko, M. M. Fang, T. Hyeon, K. J. Kolbeck, Phil. Trans. R. Soc. Lond. A, 1999, 357, 335-353

[27] V. M. Longo, L. S. Cavalcante, E. C. Paris, J. C. Sczancoski, P. S. Pizani, M. Siu Li, J. Andr es, E. Longo, and J. A. Varela, J. Phys. Chem. C, 2011, 115, 5207-5219

[28] J. Yang, C. Li, X. Zhang, Z. Quan, C. Zhang, H. Li, and J. Lin, Chem. Eur. J. 2008, 14, 4336-4345

[29] P. S. Dutta, and A. Khanna, J. Solid State Sci. Technol., 2013, 2, R3153-R3167

[30] W. Wang, L. Zhen, C. Xu, W. Sha and Z. Chen, CrystEngComm, 2013, 15, 8014-8021

[31] D. L. Wood, J.Tauc, Phys. Rev. B, 1972, 5 3144-3151

[32] T. Thongtema, S. Kungwankunakorn, B. Kuntalue, A. Phuruangrat, S. Thongtem, J. Alloys Compd., 2010, 506, 475-481

[33] X. Yang, Y. Zhou, X. Yu, H. V. Demir and X. Sun, J. Mater. Chem., 2011, 21, 9009-9013

[34] G. Jia, C. Huang, L. Li, C. Wang, X. Song, L. Song, Z. Li, S. Ding, Opt. Mater., 2012, 35,

285-291

[35] Z. Xia and D. Chen, J. Am. Ceram. Soc., 2010, 93 1397-1401

[36] L.F. Koao, F.B. Dejene, R.E. Kroon, H.C. Swart, J. Lumin. 2014, 147, 85-89

[37] J. Yang, X. Yang, H. Yang, J. Alloys Compd., 2012, 512, 190-194

[38] G. Zhu. Z. Ci, C. Ma, Y. Shi, Y. Wang, Mater. Res. Bull. 2013, 48, 1995-1998

[39] S. Long, J. Hou, G Zhang, F. Huang, Y. Zeng, Ceram. Int. 2013, 39, 6013-6017

[40] Y. Huang, Yosuke Nakai, Taiju Tsuboi, and Hyo Jin Seo, Opt. Express, 2011, 19, 6303-6311

[41] W. Zhao, S. An, B. Fan, S. Li, Y. Dai, Chin. Sci. Bull., 2012, 57, 827-831

[42] L. Li, W. Zi, G. Li, S. Lan, G. Ji, S. Gan, H. Zou, X. Xu, J. Solid State Chem., 2012, 191, 175-180

[43] J. A. Capobianco, J. C. Boyer, F. Vetrone, A. Speghini, and M. Bettinelli, Chem. Mater., 2002, 14, 2915-2921

[44] J. Yang, C. Li, Z. Quan, C. Zhang, P. Yang, Y. Li, C.Yu, and J. Lin, J. Phys. Chem. C, 2008, 112, 12777-12785

[45] C. Zhang, Z. Hou, R. Chai, Z. Cheng, Z. Xu, C. Li, L. Huang, and J. Lin, J. Phys. Chem. C 2010, 114, 6928-6936

[46] Z. Xu, S. Bian, J. Wang, T. Liu, L. Wang and Y. Gao, RSC Adv. 2013, 3, 1410-1419

[47] L. Sun, Y. Qiu, T. Liu, J. Zhang, S. Dang, J. Feng, Z. Wang, H. Zhang, and L. Shi, ACS Appl. Mater. Interfaces 2013, 5, 9585-9593

[48] D. Chen, Y. Yu, P. Huang, H. Lin, Z. Shan, L. Zeng, A. Yang and Y. Wang, Phys. Chem. Chem. Phys., 2010, 12, 7775-7778

[49] Y. Zhang, D. Geng, X. Kang, M. Shang, Y. Wu, X. Li, H. Lian, Z. Cheng, and J. Lin, Inorg. Chem., 2013, 52, 12986-12994

Figure Captions

Fig. 1. (a) The XRD patterns (b) EDS spectrum of the as-synthesized $CdMoO_4$ microspheres. (c) Nitrogen adsorption-desorption isotherm loop (d) pore-size distribution calculated from the adsorption branch by the BJH model.

Fig. 2. (a) Low- and (b) high-magnification SEM images of the $CdMoO_4$ samples.

Fig. 3. SEM images of the $CdMoO_4$ obtained by using $(NH_4)_6Mo_7O_{24}\cdot 4H_2O$ as the Mo source (a - d), $Cd(CH_3COO)_2\cdot 2H_2O$ as the Cd source (e, f).

Fig. 4. The SEM images of $CdMoO_4$ crystals prepared at different concentration of the reagents $[Cd^{2+}] = [MoO_4^{2-}] = 0.02M$ (a), 0.06M (b), 0.10M (c), and 0.14M (d), respectively.

Fig. 5. The SEM images of the products collected at different ultrasound reaction time (a) 0, (b) 5, (c) 10, (d) 15 , (e) 20 min and (f) 30 min, respectively.

Fig. 6. Schematic illustration of the possible formation mechanism for the $CdMoO_4$ samples.

Fig. 7. (a) The UV-vis diffuse reflectance spectrum. (b) the plot of $(aE_{photon})^2 \sim E$ of the $CdMoO_4$ samples.

Fig. 8. Room-temperature PL spectra of the$CdMoO_4$ samples obtained under different reactants.(a) $CdCl_2\cdot 2.5H_2O + Na_2MoO_4\cdot 2H_2O$ (b) $Cd(CH_3COO)_2\cdot 2H_2O + Na_2MoO_4\cdot 2H_2O$ (c) $CdCl_2\cdot 2.5H_2O + (NH_4)_6Mo_7O_{24}\cdot 4H_2O$.

Fig. 9. Excitation and emission spectra of $CdMoO_4:Pr^{3+}$ (a, b) $CdMoO_4:Sm^{3+}$ (c, d) $CdMoO_4:Eu^{3+}$ (e, f) $CdMoO_4:Dy^{3+}$ (g, h) samples.

Fig. 10. Emission spectra of $CdMoO_4:Ho^{3+}$ (a) $CdMoO_4:Er^{3+}$ (b) samples.

Fig. 11. Schematic diagram of MoO_4^{2-} and Ln^{3+} (Ln = Pr, Sm, Eu, Dy, Ho and Er) energy levels and excitation, emission, and energy transfer in $CdMoO_4:Ln^{3+}$ phosphors.

Fig. 12. CIE chromaticity diagram showing the emission colors for $CdMoO_4$: (A) Pr^{3+}, (B) Sm^{3+}, (C) Eu^{3+}, (D) Dy^{3+}, (E) Ho^{3+} and (F) Er^{3+}phosphors.

Table 1. Summary of the PL properties of the $CdMoO_4$: Ln^{3+} (Ln = Pr, Sm, Eu, Dy, Ho and Er) microsphere samples

Ln^{3+}	Excitation peaks(nm)/transition	Emission peaks(nm)/transition	CIE coordinates (x, y)	Colors	CCT (K)
Pr	322/CTB, 453/($^3H_4\rightarrow{}^3P_2$), 477/($^3H_4\rightarrow{}^3P_1$), 490/($^3H_4\rightarrow{}^3P_0$).	534/($^3P_0\rightarrow{}^3H_4$), 561/($^3P_0\rightarrow{}^3H_5$), 597,606/($^1D_2\rightarrow{}^3H_4$), 623/($^3P_0\rightarrow{}^3H_6$), 654/($^3P_0\rightarrow{}^3F_2$).	x=0.624 y=0.376	red	1887
Sm	339/CTB, 408/($^6H_{5/2}\rightarrow{}^4K_{11/2}$), 423/($^6H_{5/2}\rightarrow{}^6P_{5/2}+{}^4M_{19/2}$), 478/($^6H_{5/2}\rightarrow{}^4I_{11/2}+{}^4M_{15/2}$).	563/($^4G_{5/2}\rightarrow{}^6H_{5/2}$), 596,606/($^4G_{5/2}\rightarrow{}^6H_{7/2}$), 645/($^4G_{5/2}\rightarrow H_{9/2}$).	x=0.554 y=0.443	yellow	1994
Eu	330/CTB, 382/($^7F_0\rightarrow{}^5L_7$), 395/($^7F_0\rightarrow{}^5L_6$), 417/($^7F_0\rightarrow{}^5D_3$), 467/($^7F_0\rightarrow{}^5D_2$).	591/($^5D_0\rightarrow{}^7F_1$), 615/($^5D_0\rightarrow{}^7F_2$), 650/($^5D_0\rightarrow{}^7F_3$).	x=0.666 y=0.334	red	3339
Dy	330/CTB, 353/($^6H_{15/2}\rightarrow{}^6P_{7/2}$), 368/($^6H_{15/2}\rightarrow{}^6P_{5/2}$), 391/($^6H_{15/2}\rightarrow{}^4F_{7/2}+{}^4I_{13/2}$), 429/($^6H_{15/2}\rightarrow{}^4G_{11/2}$), 455/($^6H_{15/2}\rightarrow{}^4I_{15/2}$), 477/($^6H_{15/2}\rightarrow{}^4F_{2/9}$).	478, 487/($^4F_{9/2}\rightarrow{}^6H_{15/2}$), 575/($^4F_{9/2}\rightarrow{}^6H_{13/2}$).	x=0.351 y=0.360	white	4808
Ho	320/CTB, 361/($^5I_8\rightarrow{}^5G_2$), 402/($^5I_8\rightarrow{}^5G_4$), 418/($^5I_8\rightarrow{}^5G_5$), 451/($^5I_8\rightarrow{}^5F_1$), 481/($^5I_8\rightarrow{}^5F_2$).	543/($^5F_4\rightarrow{}^5I_8$), 644, 660/($^5F_5\rightarrow{}^5I_8$).	x=0.432 y=0.561	yellow	3933
Er	318/CTB, 365/($^4I_{15/2}\rightarrow{}^4G_{7/2}$), 378/($^4I_{15/2}\rightarrow{}^4G_{11/2}$), 407/($^4I_{15/2}\rightarrow{}^2H_{9/2}$), 488/($^4I_{15/2}\rightarrow{}^4F_{7/2}$).	525,531/($^2H_{11/2}\rightarrow{}^4I_{15/2}$), 545,554/($^4S_{3/2}\rightarrow{}^4I_{15/2}$), 656,668/($^4F_{9/2}\rightarrow{}^4I_{15/2}$).	x=0.275 y=0.705	green	6311

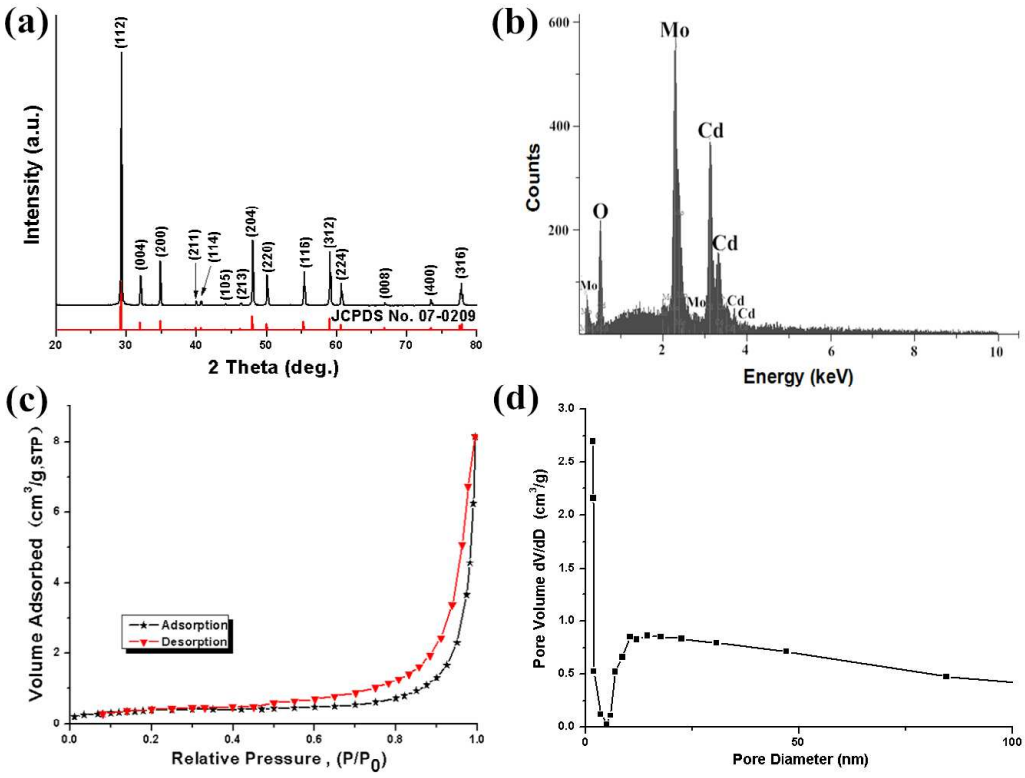

Fig. 1.

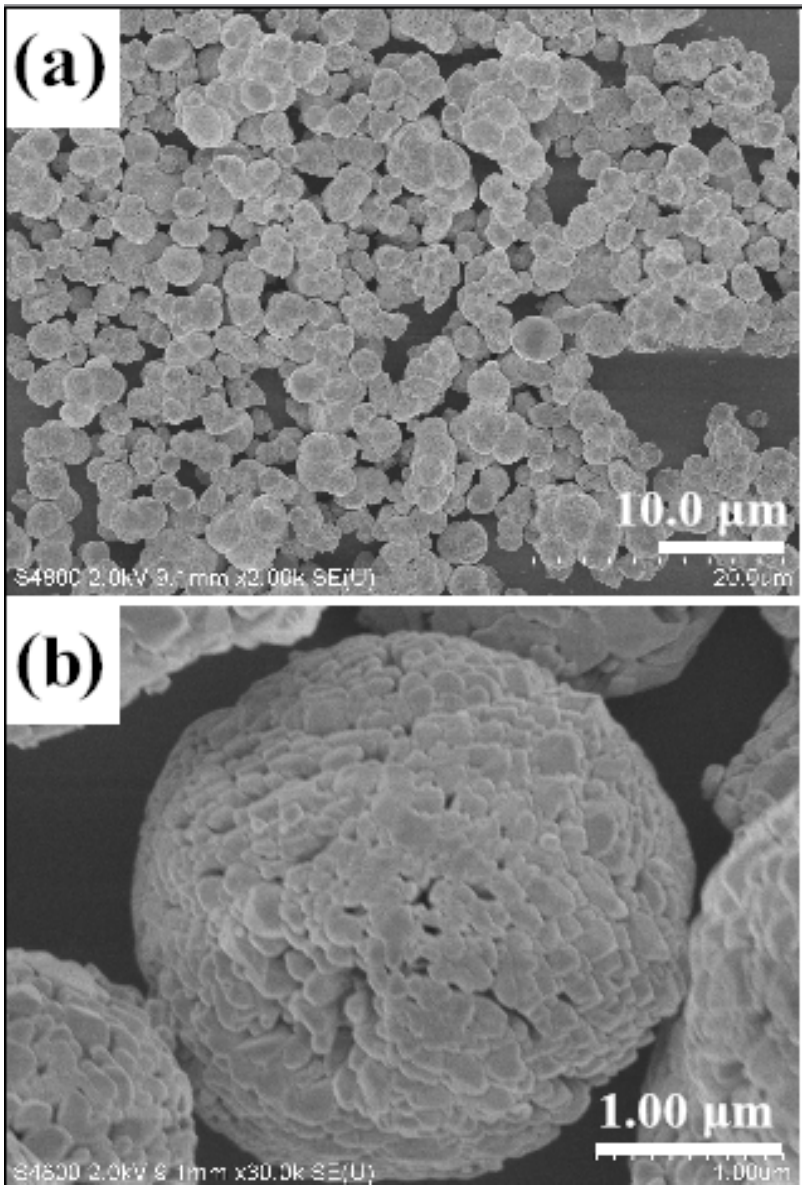

Fig. 2.

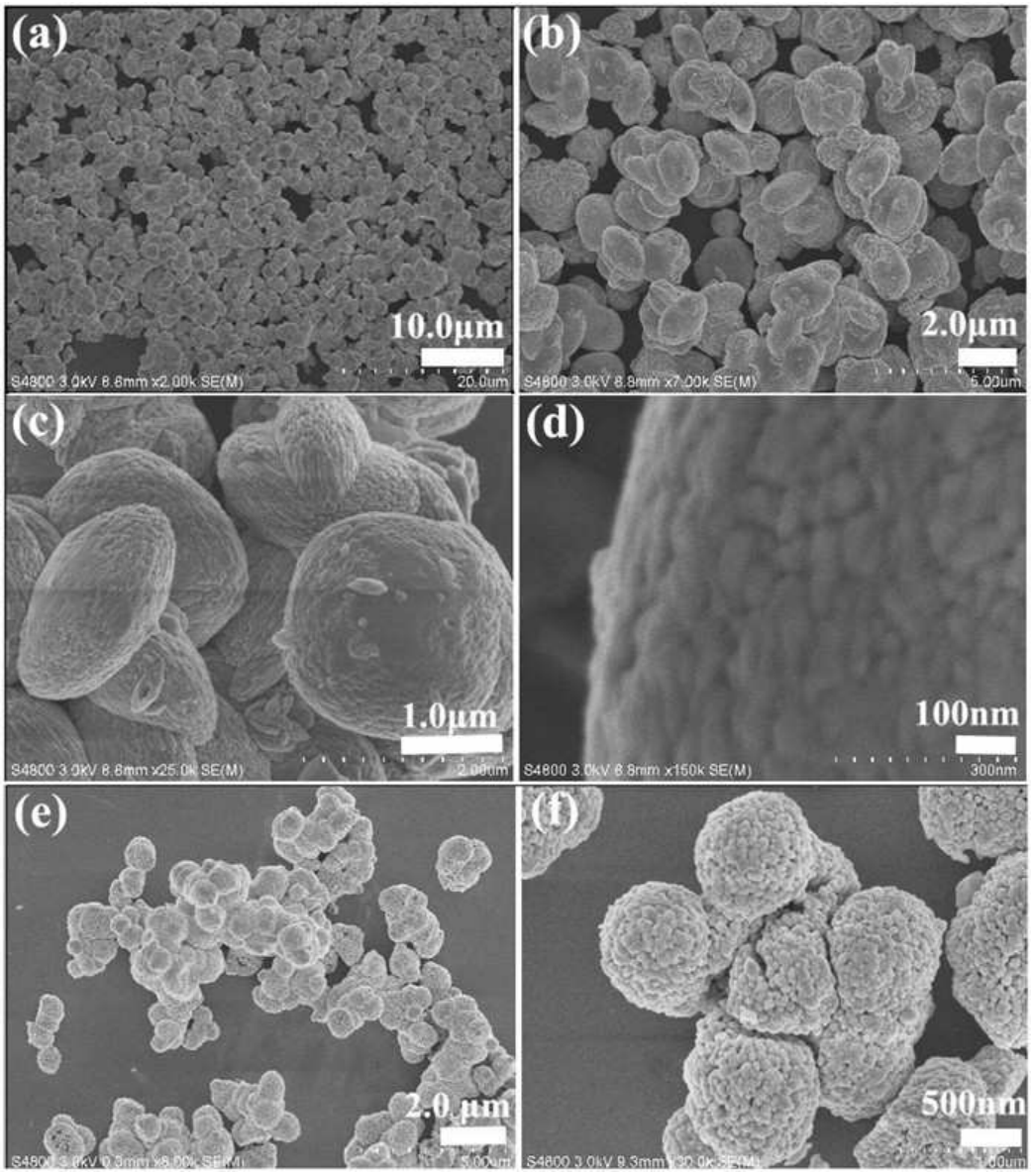

Fig. 3.

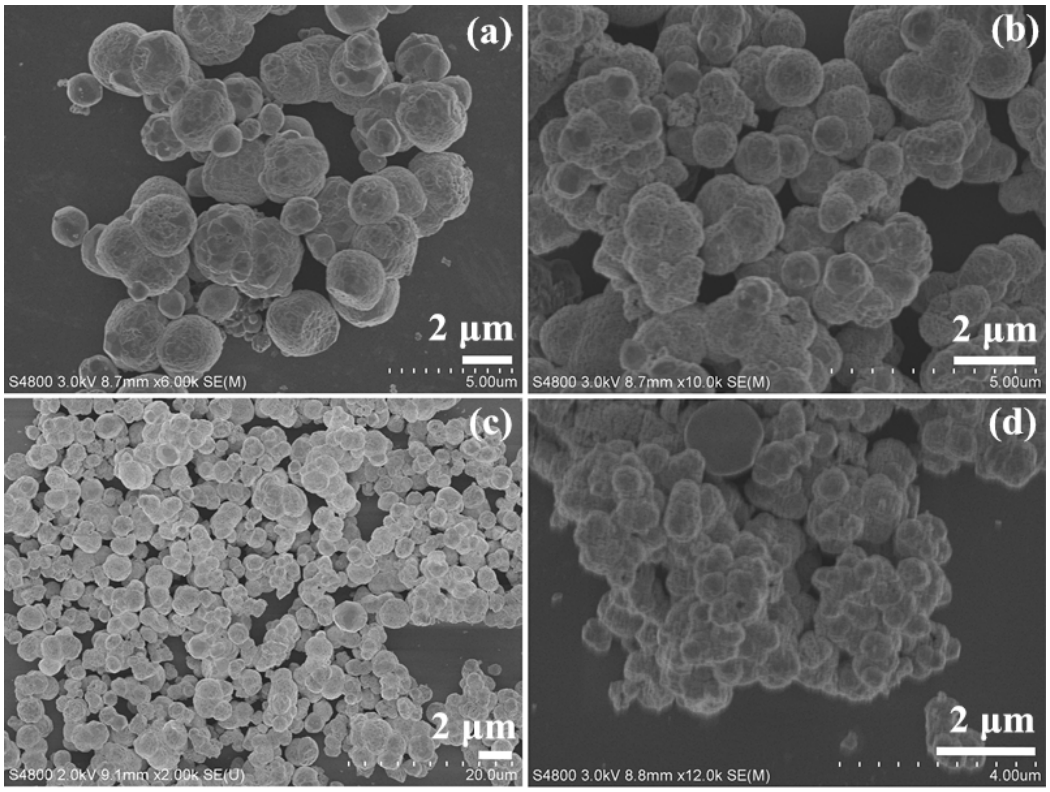

Fig. 4.

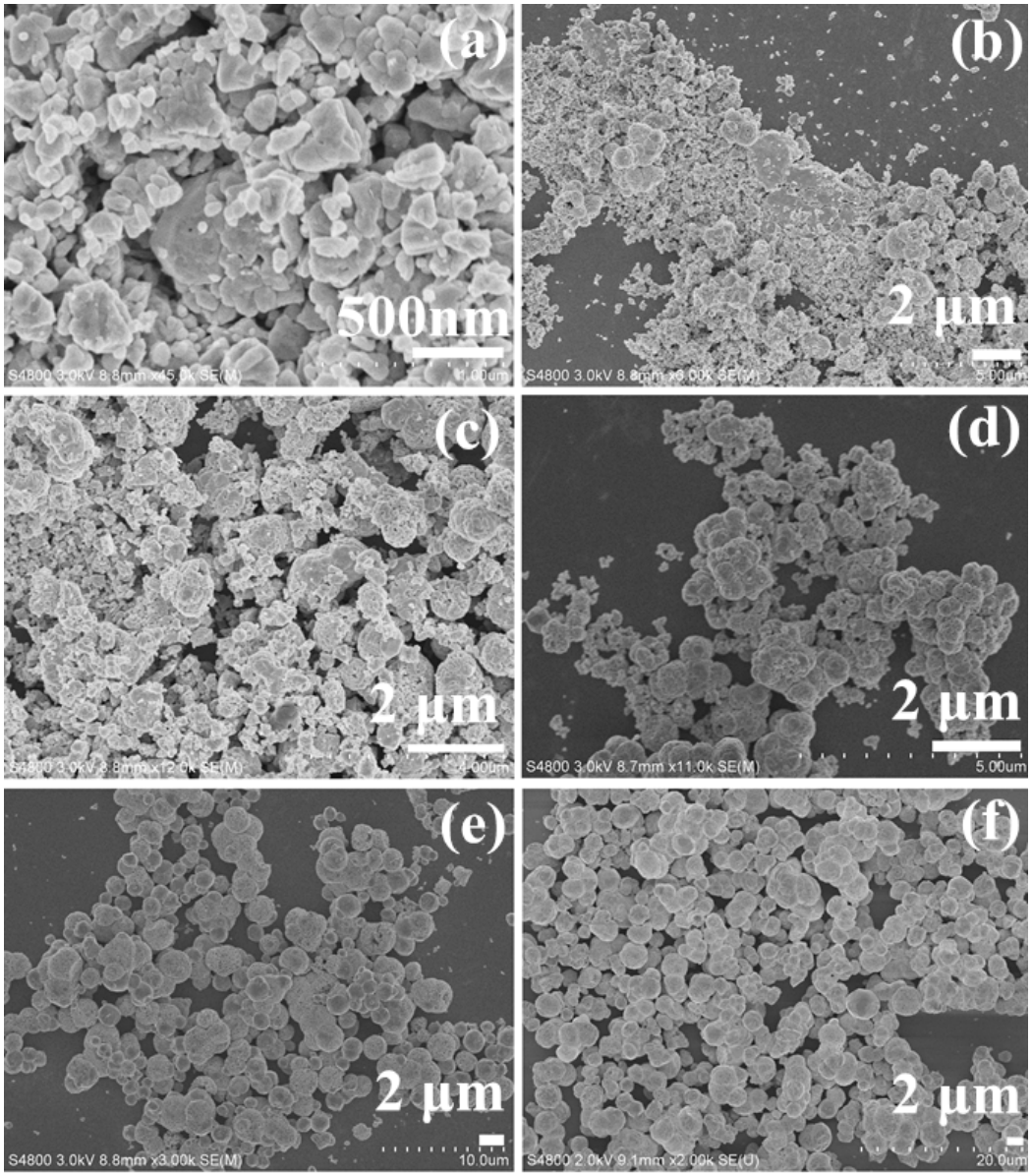

Fig. 5.

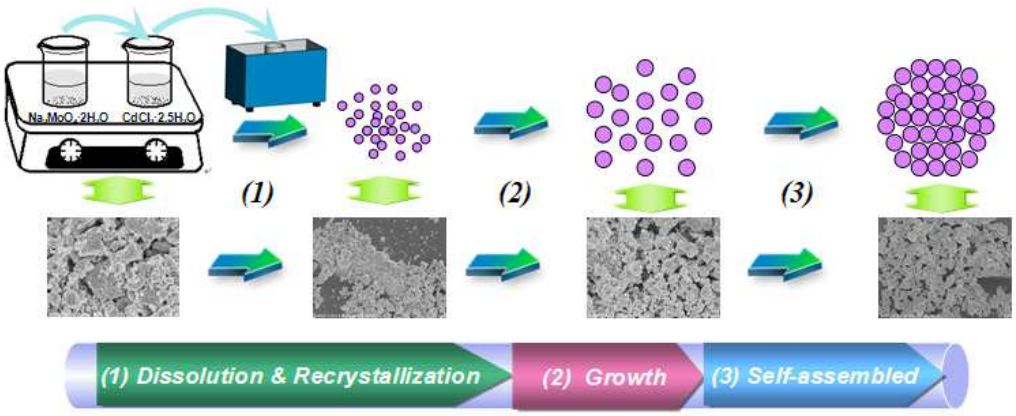

Fig. 6.

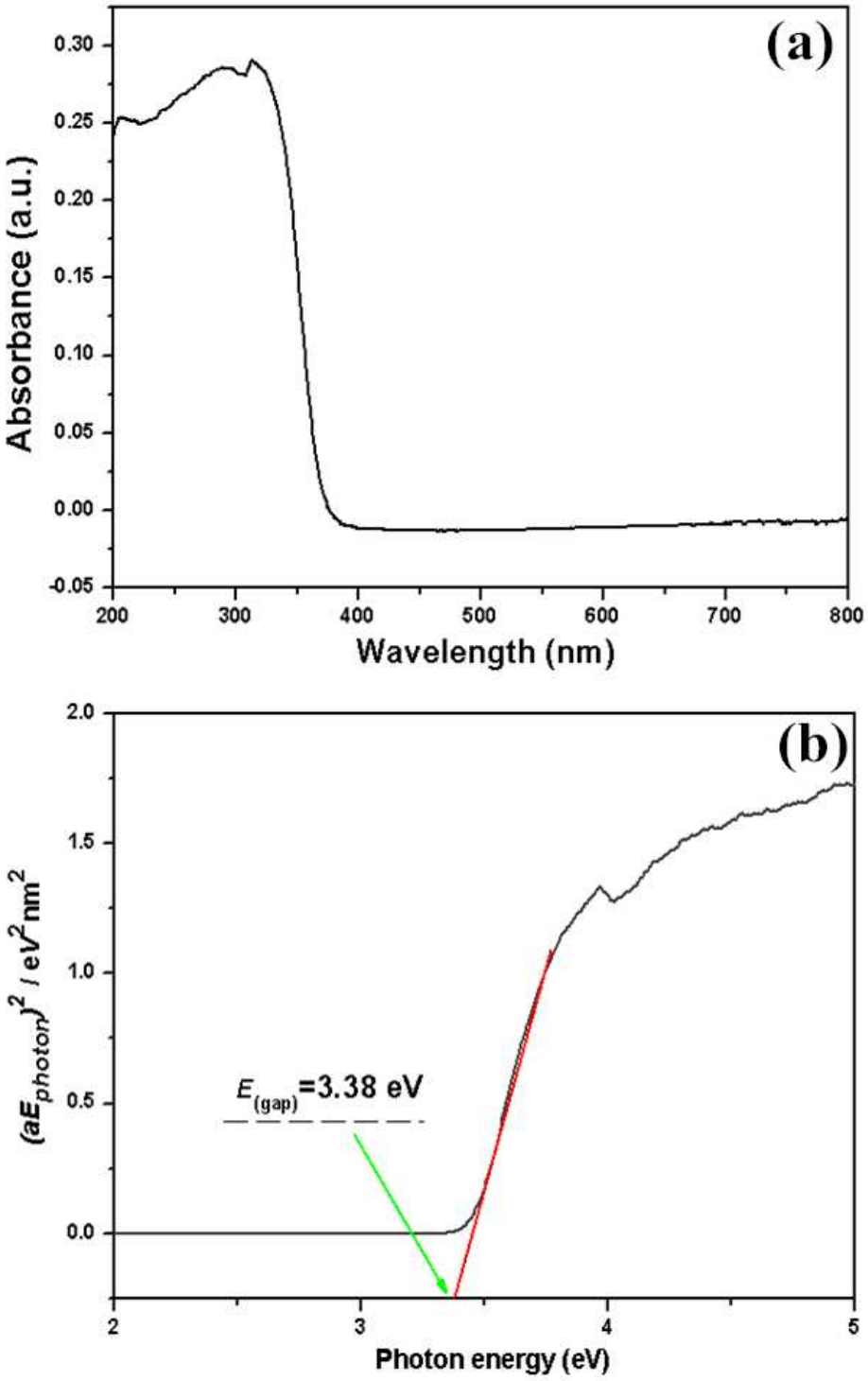

Fig. 7.

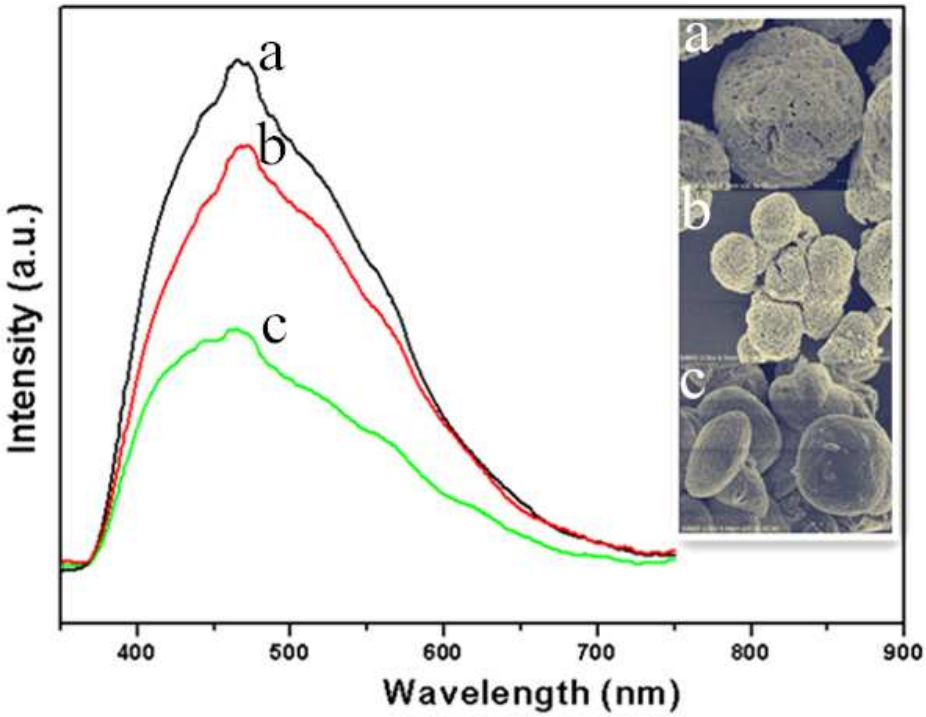

Fig. 8.

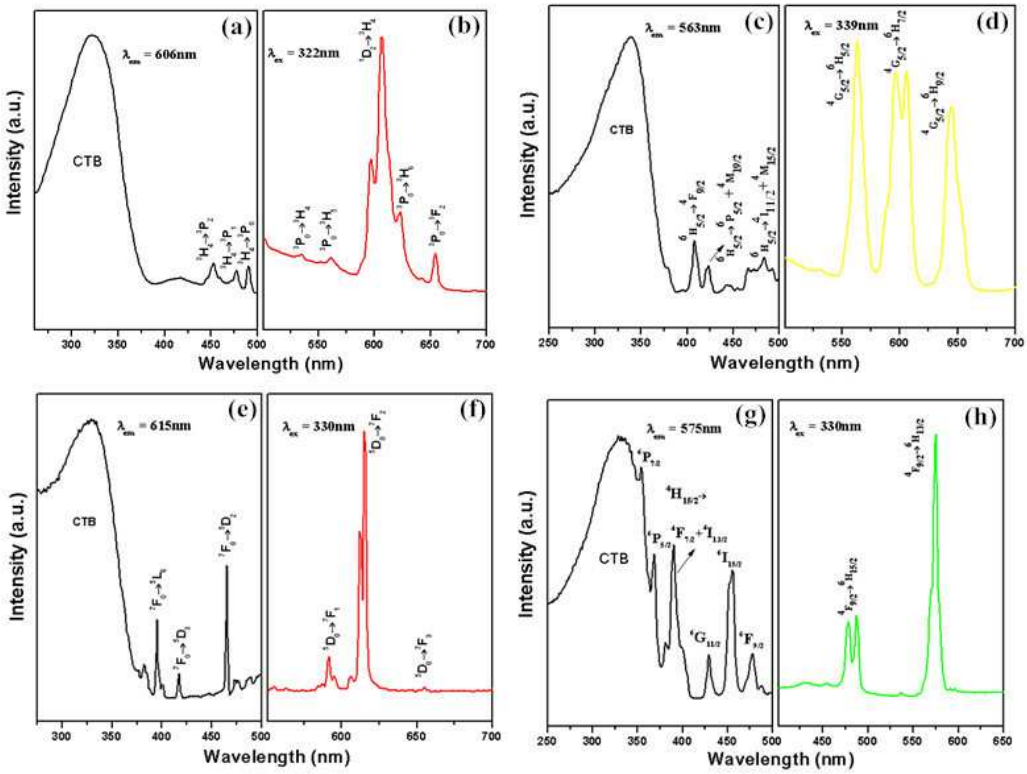

Fig. 9.

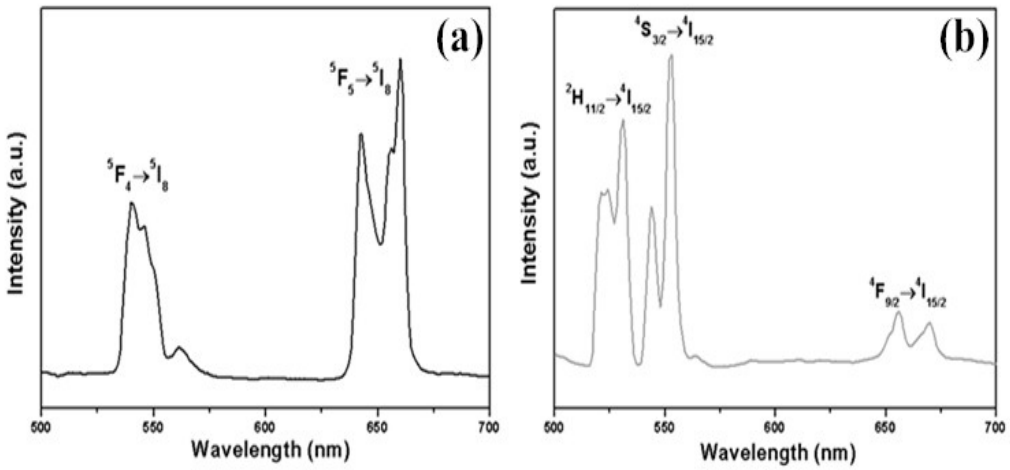

Fig. 10.

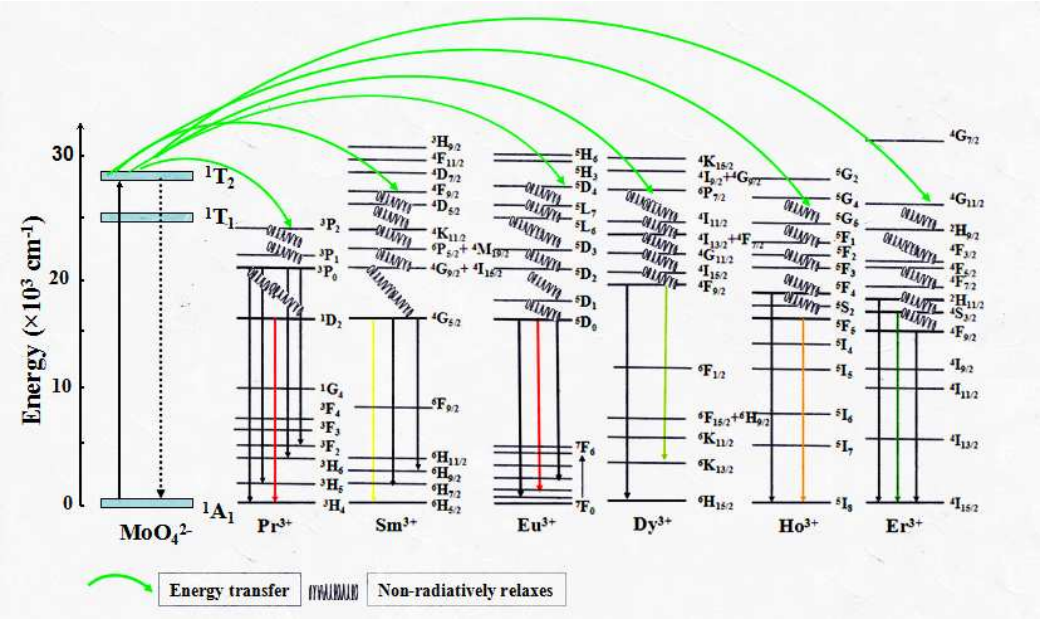

Fig. 11.

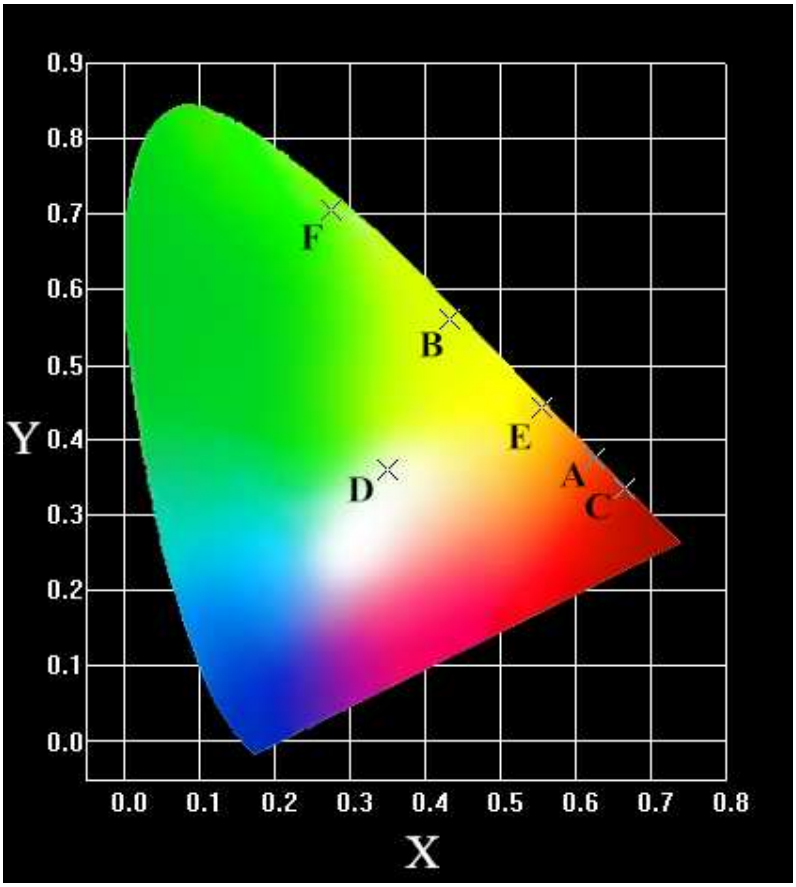

Fig. 12.